Open access • Journal Article • DOI:10.1021/ACSCATAL.6B00945

Quantifying Graphitic Edge Exposure in Graphene-Based Materials and Its Role in Oxygen Reduction Reactions — Source link

Serban N. Stamatin, Irina Hussainova, Irina Hussainova, Roman Ivanov ...+1 more authors

Institutions: Trinity College, Dublin, Tallinn University of Technology, Saint Petersburg State University of Information Technologies, Mechanics and Optics

Published on: 12 Jul 2016 - ACS Catalysis (American Chemical Society)

Topics: Electrocatalyst, Graphene and Electrochemistry

Quantifying graphitic edge exposure in graphene based materials and its role in oxygen reduction reactions

Journal:	*ACS Catalysis*
Manuscript ID	cs-2016-00945f.R1
Manuscript Type:	Article
Date Submitted by the Author:	n/a
Complete List of Authors:	Stamatin, Serban; J. Heyrovský Institute of Physical Chemistry, Academy of Sciences of the Czech Republic, Hussainova, Irina; Tallinn University of Technology, Ivanov, Roman; Tallinn University of Technology, Department of Materials Engineering Colavita, Paula; Trinity College Dublin, School of Chemistry

Quantifying graphitic edge exposure in graphene based materials and its role in oxygen reduction reactions

Serban N. Stamatin[a†], *Irina Hussainova*[b,c], *Roman Ivanov*[b], *Paula E. Colavita*[a]*

[a] School of Chemistry and Centre for Research on Adaptive Nanostructures and Nanodevices (CRANN), Trinity College Dublin, College Green, Dublin 2, Ireland

[b] Department of Materials Engineering, Tallinn University of Technology, Ehitajate 5, 19086, Tallinn, Estonia

[c] ITMO University, Kronverkskiy 49, St. Petersburg, 197101, Russia

Abstract

Oxygen electrochemistry is at the core of several emerging energy conversion technologies. The role of carbon nanostructures in the electrocatalysis of the oxygen reduction reaction is not well understood. Herein we report an investigation of the role of graphitic edges in oxygen electrochemistry. A new synthetic method was used to create all-carbon model electrode materials with controlled morphology. Electron microscopy results show that synthesized materials possess a high density of graphitic edges. Electrochemical intercalation experiments however indicate that the density of electroactive edges does not correlate positively with microscopy results. The materials were then characterized as electrodes for the oxygen reduction reaction in alkaline media. Results suggest that electrochemical determinations of edge and defect density more accurately predicts electrocatalytic activity thus suggesting that *in situ* characterization techniques are needed to understand the carbon/electrolyte interface.

KEYWORDS: graphene, electrocatalysis, graphitic edges, oxygen reduction, ORR, intercalation, defects.

Introduction

Oxygen electrochemistry plays a crucial role in the deployment of several emergent energy technologies, such as the air-cathodes in metal-air batteries and fuel cells. Polymer electrolyte membrane fuel cells (PEMFCs) are probably the most suitable candidate for powering the future automotive industry. However high cost and short lifetime are the two key drawbacks that must be overcome for PEMFC's to be widely adopted by industry. The cathode materials cost contributes significantly to the overall cost of the membrane electrode assembly: the sluggish oxygen reduction reaction (ORR), gives rise to high cathodic over-potentials that require the use of precious metal catalysts, with Pt being the preferred choice.[1]

Nanocarbons are usually used as Pt supports for fuel cell applications due to their high surface area and corrosion resistance.[2] It has been reported that the use of heteroatom-doped carbon as a support results in increased stability and activity due to catalyst-support interactions.[3-5] Heteroatom-doped carbon can also show intrinsic ORR activity which is not yet fully understood,[6,7] but that are proposed to arise from the effect of heteroatom modifications on electronic, chemical and/or morphological properties of the carbon material. Modification of carbons via functionalization or doping with heteroatoms can result in changes in the density of states and Fermi energy positioning.[1,8,9] Heteroatom modification can also create specific chemical sites at the carbon surface, thus offering new adsorption or chemisorption channels to redox species in solution. Carbon morphology may also be altered, for instance, the introduction of pyridinic groups can favor the presence of graphitic edges and thus influence the density of defects in the material.[10] Electronic, chemical and structural/morphological effects are therefore interrelated in heteroatom-modified carbons and they can all affect mechanisms and rates of

electrochemical reactions.[11] Therefore, it is often challenging to ascribe an observed change in ORR activity to a specific effect to develop new insights on optimal carbon material design.

Graphitic edge (GE) exposure is one of the carbon properties that is of great interest in electrochemistry.[12-15] Testing the electrochemical behavior of GEs is difficult because of the challenges involved in achieving well defined morphologies that are rich in edges and because of the challenges involved in characterizing GEs. Studies on ball milled graphene concluded that small graphene flakes possess a higher ORR activity than larger ones due to greater exposure of GEs.[16-18] However ball milling yields defect-rich materials that also possess oxidized surface functionalities; both of these give rise to changes in density of electronic states and lead to the presence of specific chemical sites, which can both influence ORR activity.[19] Therefore, there is a need for testing materials in which the sole effect of GE can be related to ORR activities.

GEs are usually characterized by electron microscopy methods, Raman spectroscopy and X-ray photoelectron spectroscopy. Imaging techniques are a local probing tool, while Raman and X-ray photoelectron spectroscopy offer insights on the structure and functionalities present at the carbon surface. Indeed, the electrode kinetics are influenced by oxygen functionalities,[19] hence the methods are mandatory in understanding the carbon. However, these characterization methods do not offer any information about the carbon/electrolyte interface which is the main focus of electrochemistry.

Herein, we report a novel method for the production of carbon nanostructures with controlled morphologies grown on a dielectric alumina nanofiber support. We used thus grown materials to investigate the role of GEs in oxygen reduction reactions at un-doped carbon materials, with the chief aim of understanding the effect of changes in carbon matrix structure on ORR activity. Our

results highlight the importance of establishing the density of electroactive GEs to correctly interpret ORR activity trends.

Experimental Methods

Material synthesis. The graphene layers were deposited onto a support of alumina (γ-Al_2O_3) nanofibers of 7±2 nm in diameter and specific surface area of 155 m^2 g^{-1},[20] by a one-step catalyst-free chemical vapor deposition (CVD) technique, as detailed elsewhere.[21,22] Decomposition of methane in the presence of nitrogen as carrier gas is catalyzed by unsaturated Al sites on an oxide surface and results in deposition of a carbon film at 1000 °C and atmospheric pressure. The carbon obtained via CVD wraps the alumina nanofibers forming a multi-layered graphene-like shroud along the oxide fiber. Deposition time, ratio between carbon source and carrier gas, as well as the total flow rate were controlling factors for the carbon loading and the morphology of carbon-alumina hybrid structures. In this work the dwell times were selected to be 20, 60 and 120 minutes in order to fabricate carbon materials with different morphologies used for electrochemical studies.

Characterization. The morphology of the hybrid structures was examined by high-resolution scanning electron microscopy (HR-SEM, Zeiss Gemini Ultra-55) and transmission electron microscopy (TEM JEOL JEM-2200FS). Raman spectra of the graphene layers on alumina substrates were obtained on a Horiba LabRam R800 with 532 nm laser excitation.[23] The carbon content was determined by thermogravimetric analysis (Stanton Redcroft); samples were heated in air up to 950 °C at 5 °C min^{-1}. Specific surface area measurements were carried out on a Quantachrome Autosorb iQ, running nitrogen physisorption measurements at 77 K. X-ray photoelectron spectroscopy (XPS) was performed in an Omicron Multiprobe XPS system with a

base pressure of 2×10^{-10} mbar, using a monochromatized Al Kα source (hν =1486.6 eV) and an EA125 U5 analyzer at 45° takeoff angle. Wide surveys were collected at 50 eV pass energy, while core level spectra were collected at 20 eV pass energy. Data were analyzed using CasaXPS™; high resolution spectra were Shirley background-corrected and fitted with Voigt line shapes in order to obtain area ratios.

Hydrodynamic electrochemical characterization was performed in a three-electrode glass cell setup. All the water used throughout experiments was ultrapure water (>18.2 MΩ, Millipore). The electrochemical cell was kept at 80 °C overnight in ultrapure water prior to use. A hydrogen electrode (Hydroflex®, Gaskatel) was used as reference electrode and a high purity graphite rod (99.997%, Goodfellow) was used as a counter electrode. The reference electrode potential was calibrated by performing hydrogen evolution reactions as reported in previous studies.[24] Its potential was found to be +10 mV vs. RHE (Figure S1). A rotating disk electrode (RDE, Pine Instruments) with a 0.196 cm^2 glassy carbon insert was used as a working electrode. The electrodes were polished to a mirror finish prior to use with a 50 nm alumina slurry on a polishing cloth (Buehler). The inks were formulated by dispersing 4.0 mg of the desired material in 920 µl of ultrapure water/isopropyl alcohol [1:1 (v/v)] and 80 µl of 0.05 wt. % Nafion solution. The solution was sonicated for 1 h; subsequently, a 10 µl drop was spread on the surface of the mirror polished glassy carbon. All measurements were carried out in 150 ml freshly prepared 0.1 M KOH (Semiconductor grade pellets, Sigma Aldrich). First, the electrode was conditioned by running ten cyclic voltammograms (CV) between 0.05 and 1.2 V_{RHE} at a 0.2 V s^{-1} scan rate (Metrohm potentiostat). The electrolyte was then deaerated with Ar for 30 min and an additional 5 CVs were recorded from 0.05 to 1.1 V_{RHE} and a 0.05 V s^{-1} scan rate. Oxygen reduction reactions (ORR) were recorded at 0, 400, 900 and 1600 rpm in O_2 saturated 0.1 M

KOH. In order to correct for the capacitive current, the CVs in Ar were subtracted from the ORR sweeps. The onset potential was defined as the potential where the current is 0.1 mA cm^{-2}.[25] Kinetic currents were determined from the Koutecky-Levich formula.[26] Error bars for numerical values represent 95% confidence interval.

Intercalation studies using 4-nitrobenzyl amine (4-NBA), obtained according to previously reported methods,[27] were carried out by suspending 1.0 mg of the desired material in 5 ml of a 10 mM solution of 4-NBA in acetonitrile.[28] After 3 h of incubation time, the powders were collected by centrifugation and washed 3 times with acetonitrile and water to remove excess 4-NBA. 1.0 mg of 4-NBA intercalated powders were collected and redispersed in 1 ml of acetonitrile and subsequently used as an ink. 10 µl of this ink was spread on the surface of a glassy carbon and immersed in 100 ml freshly prepared deaerated 0.1 M H_2SO_4 (>95% TraceSelect® Ultra, SigmaAldrich). Voltammetric scans for the determination of 4-NBA coverage were carried out in an all-teflon home-built electrochemical cell and a three-electrode geometry, using a saturated KCl Ag/AgCl (0.198 V vs. RHE) reference electrode (IJ Cambria) and a Pt wire as a counter electrode. All the potentials were referenced against RHE for the reported data. CVs were recorded from -0.8 to 1.2 V_{RHE} starting at 1.2 V_{RHE} at a scan rate of 0.2 V s^{-1} (Metrohm potentiostat). The second scan was used as a background scan for the integration of the charge associated with the cathodic peak between -0.3 and 0.2 V_{RHE}. Error bars for numerical values represent 95% confidence interval.

Results and Discussion

Structural and chemical characterization of graphene-coated nanofibers. Carbon electrodes used for our studies were obtained via CVD growth on alumina nanofiber

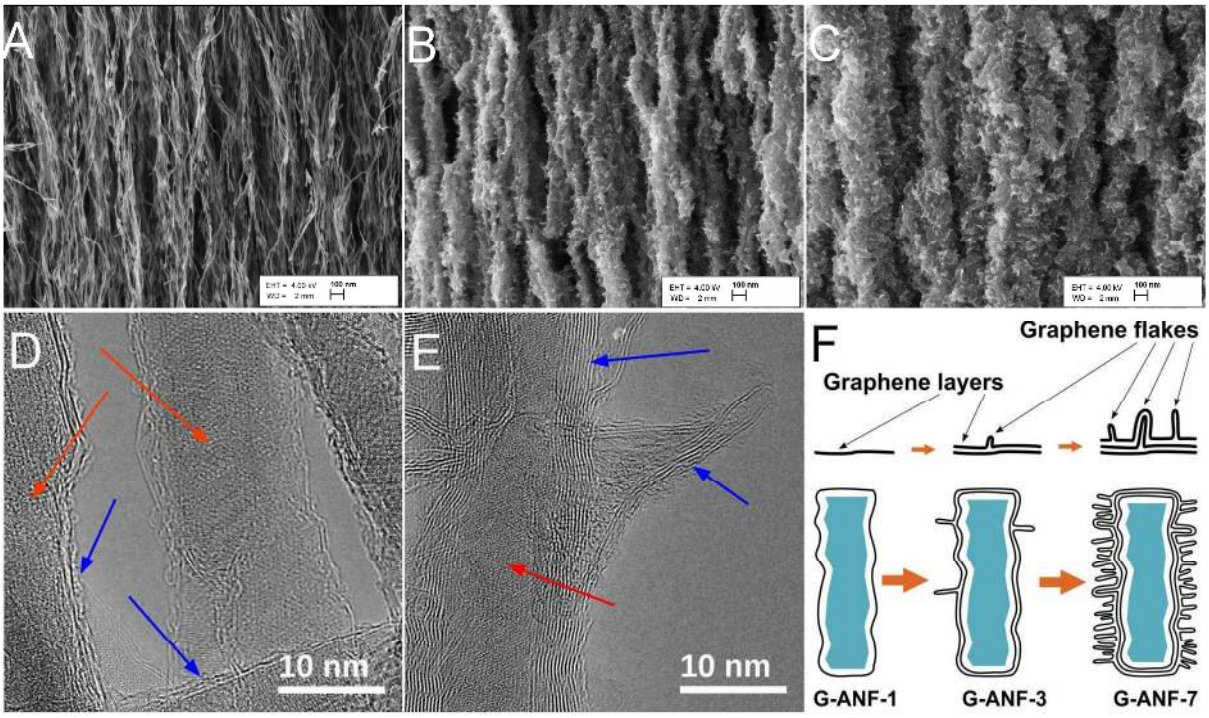

Figure 1. SEM images of G-ANF-1 (A), G-ANF-3 (B), G-ANF-7 (C) (scale bar = 100 nm); TEM images of G-ANF-1 (D) and G-ANF-3 (E) and schematic illustration of the material synthesis (F).

supports;[21,22,29] the process yielded graphene-coated alumina nanofibers (G-ANF) whereby the morphology of the carbon phase could be controlled by varying the dwell time in the CVD chamber. Figure 1 shows HR-SEM images of the samples after 20 (A), 60 (B) and 120 (C) min of processing. These samples are here onwards denoted as G-ANF-1, G-ANF-3 and G-ANF-7, respectively, according to their carbon content which is discussed below. Images in Figure 1A-C show that as the dwell time increases the width of G-ANFs increases while their walls become decorated with graphene-like flakes or protrusions. HR-TEM of G-ANF-1 and G-ANF-3 are shown in Figure 1D-E. Analysis of G-ANF-1 reveals the presence of 3-5 graphene layers oriented parallel to the long axis of the fibers and with an interspacing of 3-4 Å. Therefore, the

structure of G-ANF-1 fibers is similar to that of a multiwall carbon nanotube. As the growth process progresses, the thickness of the carbon wall increases, as evident in Figure 1E where a larger number of graphene layers parallel to the long axis can be clearly seen. The development of flakes or foliates that protrude from the fiber walls is also clearly observed in Figure 1E; these foliates are thinner than the fiber walls and consist of only 2-3 graphene layers. The microscopy analysis therefore shows that in the early stages of CVD growth the alumina fibers are coated by few graphene layers parallel to the oxide surface; longer deposition times lead to an increase in the number of these layers but also to the development of protrusions consisting of few graphene layers, as shown in the schematic in Figure 1F. Microscopy results are consistent with TGA analysis (Figure S2) that reveals that the carbon content in G-ANFs increases in the order G-ANF-1 < G-ANF-3 < G-ANF-7 and their mass gains are 15%, 300% and 700%, respectively. Interestingly, the G-ANF morphology suggests that these materials might possess a high density of exposed graphitic edges (GEs). In particular, G-ANF-3 and G-ANF-7 samples present a high density of flakes thus suggesting they could be good electrode materials with high density of sites for adsorption and fast charge transfer.

XPS analysis shows that the surface of G-ANF samples is mainly composed of carbon and oxygen as indicated by the presence of C 1s and O 1s peaks in survey spectra (Figure 2A). G-ANF-1 exhibits two additional peaks at binding energies of 74 and 119 eV which are absent in G-ANF-3 and G-ANF-7, and that can be assigned to Al 2p and 2s photoelectrons (Figure 2A). The presence of Al in G-ANF-1 samples can be attributed to the alumina (γ-Al_2O_3) support, thus indicating that G-ANF-1 has lower carbon coverage than G-ANF-3 and G-ANF-7, in agreement with TGA determinations of carbon loading. As the dwell time in the CVD chamber increases, the carbon grows uniformly leading to the complete coating of the alumina support with thicker

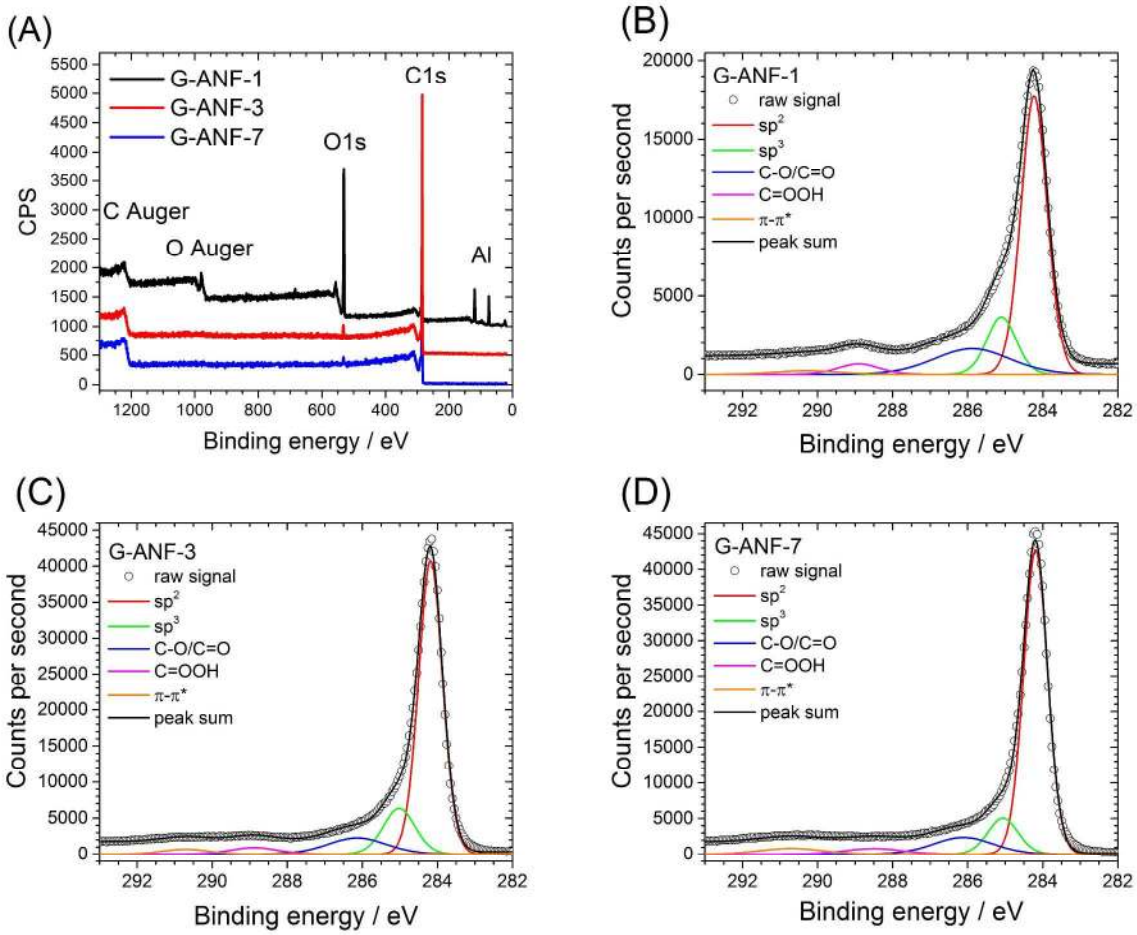

Figure 2. X-ray photoelectron spectra survey (A), high resolution of G-ANF-1 (B), G-ANF-3 (C) and G-ANF-7 (D).

carbon layers and to the disappearance of Al peaks.

Table 1 summarizes atomic ratios determined based on peak area ratios from XPS high resolution scans. The oxygen content is highest for G-ANF-1 samples, in agreement with the observation of peaks arising from the alumina support; a comparison of the O 1s peaks of G-ANF samples confirmed that the majority of the photoemitted intensity in G-ANF-1 is due to oxygen atoms from the alumina support (Figure S3, Supporting Information). The oxygen content is lowest for G-ANF-7 thus indicating that the growth process leads to the deposition of a

film with high carbon purity. The C 1s spectra exhibit a sharp peak at 284.3 eV with additional contributions at higher binding energies as shown in Figure 2B-D. A best fit of the C 1s envelope was obtained using 5 contributions at 284.3, 285.1, 286.1, 288.9 and 291.2 eV that can be attributed to trigonally bonded carbon (sp^2 centers), tetrahedrally bonded carbon (sp^3 centers), C-O/C=O carbon, carboxylic acid groups and π-π^* shake up peaks, respectively.[29] A summary of the % composition for sp^2, sp^3 and oxidised carbon centers is reported in Table 1. The sp^3 contribution remains constant at ~15% for all samples, however, the sp^2 concentration increases from 63% for G-ANF-1 to 70 and 69% for G-ANF-3 and G-ANF-7, respectively. The lower sp^2 concentration in G-ANF-1 occurs in parallel with a higher concentration of oxidized carbon centers (20%); thus suggesting that the slightly lower graphitic content at the early stages of the carbon growth might be due to chemical interactions between carbon and the oxide support.

Table 1. Summary of surface concentration (at.%) determined from XPS analysis

				C 1s		
	C%	**O%**	**Al%**	sp^2%	sp^3%	ox.C%
G-ANF-1	52	28	20	63	15	20
G-ANF-3	97	3	0	70	14	13
G-ANF-7	99	1	0	69	14	12

Figure 3 shows Raman spectra of G-ANF-1, G-ANF-3 and G-ANF-7. The main features in Raman spectra of carbons are the D and G peaks, at ~1350 and ~1590 cm^{-1}, respectively,[30] which are characteristic of carbon materials. Additional peaks at 2680, 2930 and 3230 cm^{-1} can be assigned to 2D, D+D' and 2D' bands, respectively, which are characteristic of graphene layers.[23]

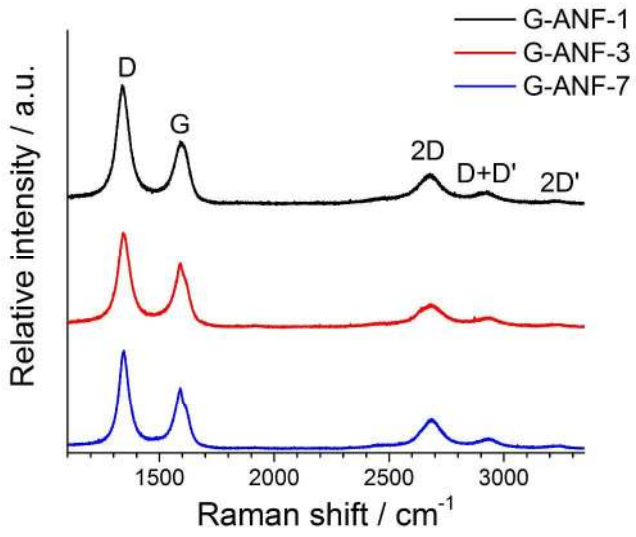

Figure 3. Raman spectra (exc. 532 nm) of G-ANF-1 (black), G-ANF-3 (red) and G-ANF-7 (blue). All spectra are normalized by the height of the G peak to facilitate comparison.

The presence of a single symmetric peak at 2680 cm^{-1} indicates that G-ANFs mostly consist of few-layer graphene, as this peak splits into an asymmetric doublet in the case of graphite;[30] moreover, the relatively narrow bands suggest the layers and foliates possess nanocrystalline structure.[23] The D peak is due to the breathing modes of carbon rings and requires defects for its activation;[23] the D band intensity may be used to quantify disorder in structures.[31] The ratio between intensities of the D and G peaks, I_D/I_G, can be used for comparing the amount of structural defects/edges and the degree of graphitization. The value of I_D/I_G is highest at 1.9 for G-ANF-1 and decreases to 1.4 for both G-ANF-3 and G-ANF-7; this suggests that the first few layers deposited at shorter dwell times are more defective than those deposited at later stages in the CVD process. A similar trend is obtained if peak height ratios are used in this analysis. This is likely due to the close interaction between the first few layers and the support; as the thickness

of the carbon wall grows, subsequent layers are deposited on an all-carbon surface and allow for larger crystallite size.

Finally, the BET surface areas determined from N_2 adsorption isotherms was found to decrease with increasing carbon content, from 203 $m^2 g^{-1}$ for G-ANF-1 to 125 $m^2 g^{-1}$ for G-ANF-3 and 119 $m^2 g^{-1}$ for G-ANF-7. In summary, this synthetic strategy yields carbon nanofibers with carbon walls consisting of few layers of graphene and with graphene foliates that protrude and expose graphitic edges at the carbon interface.

Electrochemical characterization of graphene-coated nanofibers. G-ANF materials offer an opportunity to study the electrochemical performance of metal- and dopant-free highly graphitic materials that are rich in graphitic edges (GEs). In this context, we decided to test these materials as model catalysts for understanding the role of GEs in the electrochemical reduction of water at nanostructured carbon electrodes, a matter yet to be understood.[26,32-34] We also carried out measurements on glassy carbon (GC) for comparing the performance of G-ANFs to a standard graphitic carbon electrode material.

Cyclovoltammetric scans of glassy carbon (GC), G-ANF-1, G-ANF-3 and G-ANF-7 are featureless in Ar-saturated 0.1 M KOH (Figure 4A-D). Among all the samples, G-ANF-1 has the highest capacitive current contributions, followed by G-ANF-3 and G-ANF-7. The observed trend in capacitive currents mirrors the measured BET areas, with G-ANF-1 being the material with the largest BET area and the largest capacitive contribution in its CV. All samples exhibit a dramatic increase in current around 0.75 V_{RHE} in O_2-saturated electrolyte compared to the currents observed in Ar-saturated electrolyte (Figure 4B-D). This increase around 0.75 V_{RHE} in

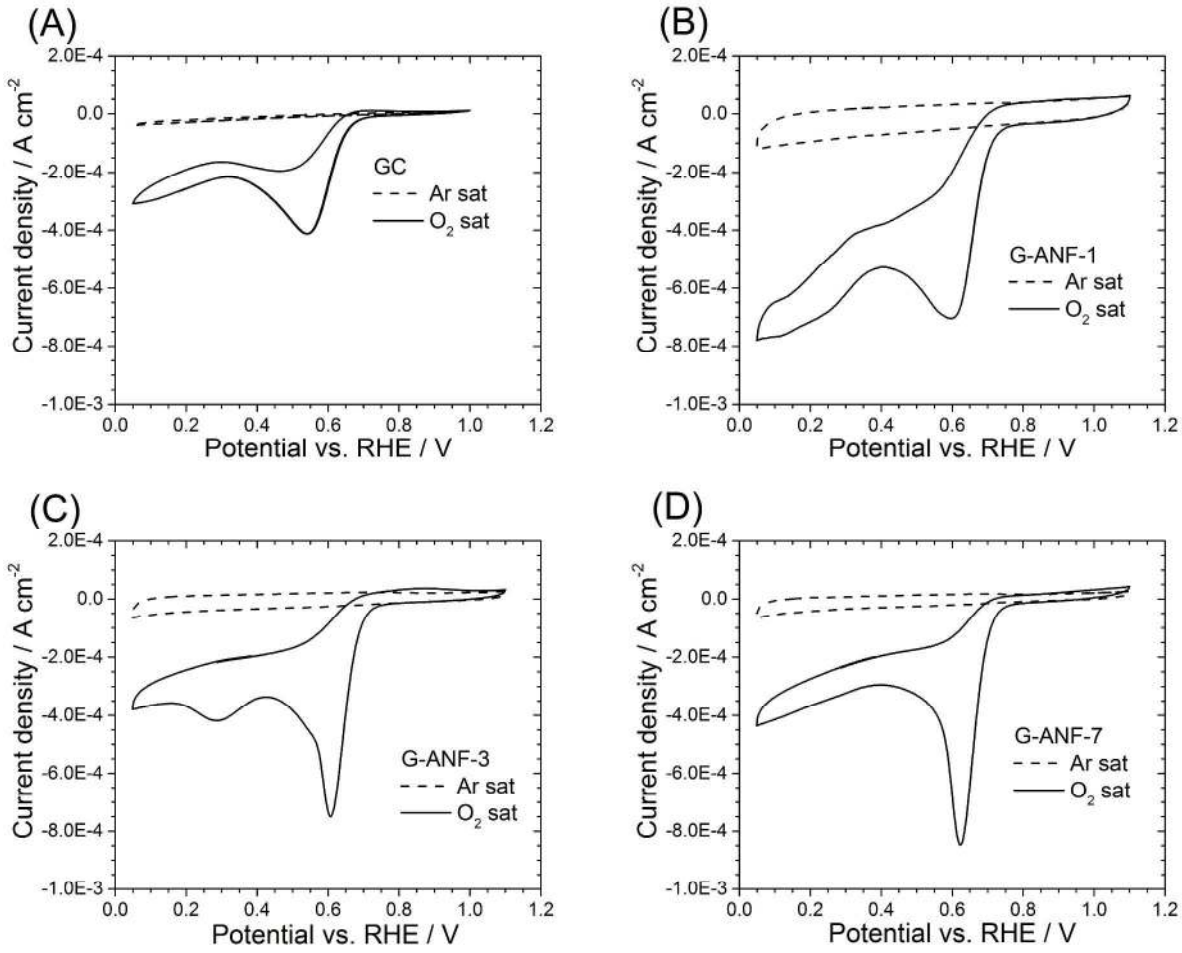

Figure 4. Cyclovoltametric scans of GC (A), G-ANF-1 (B), G-ANF-3 (C) and G-ANF-7 (D) in Ar (dashed line) and O_2 (solid line) saturated 0.1 M KOH; recorded between 0.05 and 1.1 V_{RHE} at 0.05 V s^{-1} and 25 °C.

O_2 saturated electrolyte corresponds to the electrochemical reduction of oxygen to water. Glassy carbon (Figure 4A) shows a similar peak at 0.65 V_{RHE} in O_2 saturated electrolyte, however the total current is half the value observed for G-ANF samples.

A comparison of the ORR cathodic sweeps obtained using the rotating disk electrode (RDE) method is shown in Figure 5. All samples exhibit a two-step reduction, one around 0.75 V_{RHE} and another one around 0.35 V_{RHE} corresponding to a two-step electrochemical reduction of O_2

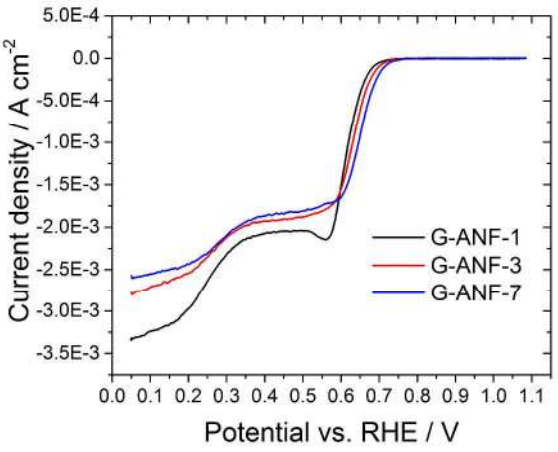

Figure 5. Cathodic voltammetric waves of G-ANF-1 (black line), G-ANF-3 (red line) and G-ANF-7 (blue line) recorded in O_2 saturated 0.1 M KOH between 0.05 and 1.1 V_{RHE} at 0.05 V s^{-1}, 900 rpm and 25 °C. All waves are shown after subtraction of capacitive contributions.

to H_2O.[9] All samples exhibit a plateau in the range 0.35-0.55 V_{RHE}, similar to a limiting current. The region between 0.35 and 0.55 V_{RHE} is diffusion controlled and the measured current is directly proportional to the number of electrons and rotation speed (see Koutecky-Levich section in Supporting Information).[35,36] For curves obtained at the same rotation speed, a higher current indicates greater selectivity towards the four electron reduction of oxygen to water. The highest current density at 0.4 V_{RHE}, was observed for G-ANF-1 electrodes indicating a higher selectivity towards the four electron reduction of oxygen as explained in the Koutecky-Levich section of the SI. All samples were found to display mixed $2e^-/4e^-$ kinetics; trends in the average e^- numbers, which are summarized in Table 2, suggest that whereas G-ANF-7 and G-ANF-3 favor the production of hydrogen peroxide ($2e^-$ reduction), G-ANF-1 favors a $4e^-$ reduction of oxygen to water. The observation of higher e^- numbers for G-ANF-1 is somewhat surprising, considering

that morphological studies show that G-ANF-1 consists of a relatively smooth carbon coating without visible evidence of a high density of reactive GE structures.

The potential at 0.1 mA cm^{-2}, also known as onset potential, averaged over 6 independent measurements was found to be similar for all samples, as reported in Table 2. The potential at half current was also found to be comparable among all samples. The most noticeable difference among the electrodes was observed for the kinetic current densities determined as shown in the Supporting Information. The mass-transport-corrected kinetic current density was determined using the following formula in the Koutecky-Levich plots (Figure S3):

$$\frac{1}{j} = \frac{1}{j_k} + \frac{1}{B\omega^{1/2}} \qquad (1)$$

where j is the measured current, j_k is the kinetic current, B is the Levich constant and ω is the angular velocity. The linear extrapolation on the y-axis yields the reciprocal kinetic current at infinite rotation. G-ANF-7 yielded the highest kinetic current density, followed by G-ANF-3 and G-ANF-1. It is important to consider, however, that despite all samples possessing identical geometric area and mass loading, the carbon mass loading is different for the three G-ANFs: G-ANF-7 has the highest carbon ratio while G-ANF-1 has the lowest carbon ratio (Figure S2). Therefore, to compare activity among samples the kinetic current density was normalized by the carbon mass, which is the electroactive fraction of the material, to obtain a mass activity, in analogy to that obtained for carbon supported catalysts.[37,38] When comparing mass-normalized kinetic currents, G-ANF-1 was found to possess the highest electrocatalytic activity.

It is interesting to notice that the trends in reactivity point at G-ANF-1 as the material that shows greatest catalytic activity; this is in agreement with analysis of Raman spectra which suggests that G-ANF-1 is the most defective of the three graphene-coated fibers and therefore

Table 2. Summary of kinetic data as obtained from hydrodynamic voltammograms.

	Onset potential* (V)	Potential at half current (V)	Kinetic current density (mA cm^{-2})	Mass activity (A g^{-1})	No. of e^-
G-ANF-1	0.73 ± 0.01	0.63 ± 0.01	1.3 ± 0.2	35.0	3.2 ± 0.3
G-ANF-3	0.72 ± 0.01	0.63 ± 0.01	1.8 ± 0.2	11.6	2.6 ± 0.5
G-ANF-7	0.73 ± 0.01	0.65 ± 0.01	2.3 ± 0.3	12.8	2.5 ± 0.6

* Potential at which the current is 0.1 mA cm^{-2}

likely to be the most edge-rich among them. However, Raman does not provide information on the amount of edges that are actually available at the carbon/electrolyte interface as it takes into account also the carbon-alumina interface which is likely distorted or defect-rich. In order to directly compare the density of electrochemically exposed GEs among the three materials, intercalation studies using 4-nitrobenzylamine (4-NBA) were carried out.[27] This method was developed by Compton and co-workers[27] for graphite and carbon nanotubes and has previously been used in our laboratory for comparing exposed GE densities at amorphous carbon electrodes.[28] Briefly, partial intercalation of 4-NBA occurs at GEs where the interlayer spacing in graphite does not allow for a full intercalation, thus leaving nitroaryl moieties exposed to the electrolyte and available for electroreduction to arylamines. The integrated electroreduction currents can then be used to compare relative GE densities among the samples.

Figure 6A shows the first two cycles in the CV of intercalated G-ANF-1 in 0.1 M H_2SO_4. The CV starts at large potentials, 1.2 V_{RHE}, and is featureless until it reaches 0.15 V_{RHE} where the reduction of Ph-NO_2 takes place until approx. -0.2 V_{RHE}. This peak can be observed only in the first scan and it corresponds to the reduction of the aromatic nitro compound.[27] In the following

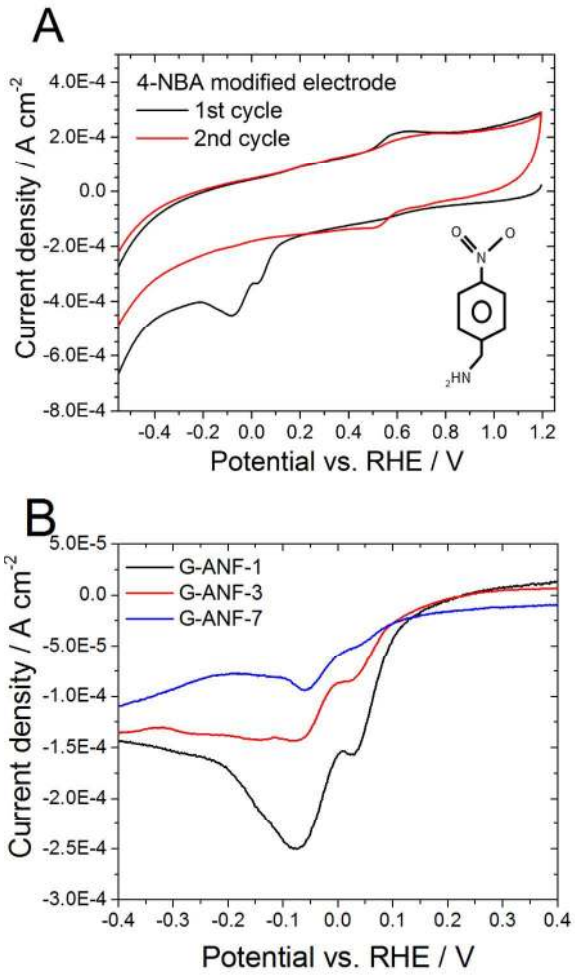

Figure 6. Cyclovoltammetric scans of a 4-NBA modified electrode (A) and 4-NBA modified G-ANF-1 (black line), G-ANF-3 (red line) and G-ANF-7 (blue line) (B) recorded in Ar saturated 0.1 M H_2SO_4 between 1.2 and -0.8 V_{RHE} at 0.2 V s^{-1}. Curves in (B) are shown after correction by background current to facilitate comparison.

scan, there is only a pair of peaks at ~0.6 V_{RHE} which appear to be quasireversible and that can be attributed to the formation of Ar-NHOH.[27,39]

The voltammetric response for G-ANF-1 is significantly larger than for the other two materials and, correspondingly, the largest electroreduction charge per unit area was found to be associated

to G-ANF-1. Integration of the reduction peak yields surface coverage for 4-NBA, Γ_{NBA}, of (4.79 ± 0.8), (3.22 ± 0.73) and (2.75 ± 1.1) x 10^{-11} mol cm^{-2} for G-ANF-1, G-ANF-3 and G-ANF-7, respectively. The obtained values of Γ_{NBA} for G-ANF-3 and G-ANF-7 are similar, however there is a considerable difference when compared to G-ANF-1. The highest Γ_{NBA} observed for G-ANF-1 indicates that the density of exposed GEs for this electrode is the highest among the three.

Analysis via microscopy would suggest that G-ANF-3 and G-ANF-7 are richer in graphitic edges given the abundant presence of foliates at the carbon surface; XPS analysis also indicated that G-ANF-3 and G-ANF-7 are richer in sp^2 content than G-ANF-1. Accordingly, based on typical trends in carbon electrodes,[11] G-ANF-3 and G-ANF-7 could have been expected to display faster charge-transfer than G-ANF-1 and higher electrocatalytic activity towards ORR.[17] Nevertheless, Raman spectroscopy showed that G-ANF-1 is the richest in defects among the three materials; these defects are likely to be in the form of edges/boundaries on the basal graphene plane and not visible via microscopy. Raman spectroscopy cannot distinguish among electroactive and electroinactive defect sites.

In contrast, the partial intercalation of 4-NBA directly probes GEs exposed at the carbon/electrolyte interface. This method provides information on electroactive sites and takes into account defects and GEs that directly and unambiguously contribute to the electrochemical performance of the material; this method was found to indeed correlate positively with ORR activity (see Figure S5, Supporting Information). The use of electrochemical tools, that can directly probe the role of structural changes on reactions at the carbon/electrolyte interface, appear to thus be essential to complement microscopy and to accurately relate carbon properties to electrocatalytic activity.

It should be noted that the values of onset potential and potential half maximum obtained for ORR at G-ANFs are similar to values reported for heteroatom-doped graphene and carbon nanotube composites.[17,40] Our results reveal that it is possible to modulate ORR activity and achieve high onset potentials by manipulating the properties of the carbon matrix exclusively, in the absence of heteroatom dopants. This suggests that the kinetics are not governed by heteroatom doping levels alone, but that the carbon matrix structure can critically affect catalytic activity and potentially mimic or mask the effects of any chemical doping of the carbon material. Therefore, these findings indicate that it is important to conduct experiments at undoped, pure carbon electrodes with different carbon matrix properties such as GE density to elucidate the individual roles of chemical site and carbon matrix.

Conclusions

A CVD technique was used to grow carbon electrode materials with three different morphologies. XPS revealed that the material was highly graphitic in content whereas scanning and transmission electron microscopy showed that in the initial deposition stage the substrate was wrapped by a few layers of graphene while longer synthesis times produced nanocarbons with a high density of protrusions with exposed few-layer graphene. Long CVD deposition time also results in a thicker and less defective carbon phase.

This growth method was used to fabricate three different types of electrodes that allowed us to investigate the role of defects and edges in ORR catalysis at undoped carbon electrodes. All three materials were found to display ORR onset potentials that are comparable to many N-doped carbon materials reported in the literature. Interestingly, the material that appears to be morphologically smooth when examined via microscopy, was found to be the best performer in

terms of mass activity and number of electrons involved in the reduction process. Raman and electrochemical intercalation studies suggest that this is the most defect-/edge-rich material, a structural difference that we propose accounts for its higher ORR activity. An important implication of these results is the fact that it is possible to modulate ORR activity through control of the carbon matrix to achieve catalytic performance comparable to that obtained via heteroatom doping. Careful study of matrix and doping effects in isolation might therefore be necessary to fully understand synergistic matrix-dopant effects in ORR and to translate those into tailored design of metal-free ORR catalysts. Such studies are necessary for building a rational foundation for the tailoring of carbon electrode materials for Pt-free electrocatalysis of the oxygen reduction reaction in polymer electrolyte fuel cells, metal-air batteries, and similar technologies.

ASSOCIATED CONTENT

Supporting Information. Calibration of Hydroflex® reference against RHE, thermogravimetric analysis, O 1s spectra, Koutecky-Levich plots and intercalation data. This material is available free of charge via the Internet at http://pubs.acs.org.

AUTHOR INFORMATION

Corresponding Author

* colavitp@tcd.ie

Present Addresses

† Present address: J. Heyrovsky Institute of Physical Chemistry of the CAS, Prague, Czech Republic.

Author Contributions

The manuscript was written through contributions of all authors. All authors have given approval to the final version of the manuscript.

Funding Sources

This publication has emanated from research conducted with the financial support of Science Foundation Ireland under Grant Number 13/CDA/2213. This research was also supported by the Estonian Research Council under PUT1063.

ACKNOWLEDGMENT

This publication has emanated from research conducted with the financial support of Science Foundation Ireland under Grant Number 13/CDA/2213. This research was also supported by the Estonian Research Council under PUT1063 (I. Hussainova). Use of XPS instrument of I.V. Shvets and C. McGuinness provided under SFI Equipment Infrastructure Funds. The authors would like to acknowledge Dr. Valdek Mikli and Dr. Taavi Raadik, both from Department of Materials Science, TUT, for their help with SEM imaging and Raman spectroscopy analysis. The authors are also grateful to Prof. W. Schmitt and Dr. A. Rafferty for access to instrumentation.

REFERENCES

(1) Wang, D.-W.; Su, D. *Energy Environ. Sci.* **2014**, *7*, 576-591.

(2) Trogadas, P.; Fuller, T. F.; Strasser, P. *Carbon* **2014**, *75*, 5-42.

(3) Arrigo, R.; Schuster, M. E.; Xie, Z.; Yi, Y.; Wowsnick, G.; Sun, L. L.; Hermann, K. E.; Friedrich, M.; Kast, P.; Hävecker, M.; Knop-Gericke, A.; Schlögl, R. *ACS Catal.* **2015**, *5*, 2740-2753.

(4) Ma, J.; Habrioux, A.; Alonso-Vante, N. *ChemElectroChem* **2014**, *1*, 37-46.

(5) Perini, L.; Durante, C.; Favaro, M.; Perazzolo, V.; Agnoli, S.; Schneider, O.; Granozzi, G.; Gennaro, A. *ACS Appl. Mater. Interfaces* **2015**, *7*, 1170-1179.

(6) Rao, C. V.; Cabrera, C. R.; Ishikawa, Y. *J. Phys. Chem. Let.* **2010**, *1*, 2622-2627.

(7) Zhang, L.; Xia, Z. *J. Phys. Chem. C* **2011**, *115*, 11170-11176.

(8) Wiggins-Camacho, J. D.; Stevenson, K. J. *J. Phys. Chem. C* **2009**, *113*, 19082-19090.

(9) Yang, Z.; Ren, J.; Zhang, Z.; Chen, X.; Guan, G.; Qiu, L.; Zhang, Y.; Peng, H. *Chem. Rev.* **2015**, *115*, 5159-5223.

(10) Maldonado, S.; Morin, S.; Stevenson, K. J. *Carbon* **2006**, *44*, 1429-1437.

(11) McCreery, R. L.; McDermott, M. T. *Anal. Chem.* **2012**, *84*, 2602-2605.

(12) Ubnoske, S. M.; Raut, A. S.; Brown, B.; Parker, C. B.; Stoner, B. R.; Glass, J. T. *J. Phys. Chem. C* **2014**, *118*, 16126-16132.

(13) Yoo, E.; Kim, J.; Hosono, E.; Zhou, H.-s.; Kudo, T.; Honma, I. *Nano Lett.* **2008**, *8*, 2277-2282.

(14) Yu, D.; Dai, L. *J. Phys. Chem. Let.* **2010**, *1*, 467-470.

(15) Zhang, J.; Xia, Z.; Dai, L. *Sci. Adv.* **2015**, *1*, 1500564.

(16) Benson, J.; Xu, Q.; Wang, P.; Shen, Y.; Sun, L.; Wang, T.; Li, M.; Papakonstantinou, P. *ACS Appl. Mater. Interfaces* **2014**, *6*, 19726-19736.

(17) Deng, D.; Yu, L.; Pan, X.; Wang, S.; Chen, X.; Hu, P.; Sun, L.; Bao, X. *Chem. Commun.* **2011**, *47*, 10016-10018.

(18) Jeon, I.-Y.; Choi, H.-J.; Jung, S.-M.; Seo, J.-M.; Kim, M.-J.; Dai, L.; Baek, J.-B. *J. Am. Chem. Soc.* **2013**, *135*, 1386-1393.

(19) Chen, P.; Fryling, M. A.; McCreery, R. L. *Anal. Chem.* **1995**, *67*, 3115-3122.

(20) Aghayan, M.; Hussainova, I.; Gasik, M.; Kutuzov, M.; Friman, M. *Thermochim. Acta* **2013**, *574*, 140-144.

(21) Ivanov, R.; Hussainova, I.; Aghayan, M.; Drozdova, M.; Pérez-Coll, D.; Rodríguez, M. A.; Rubio-Marcos, F. *J. Eur. Ceram. Soc.* **2015**, *35*, 4017-4021.

(22) Ivanov, R.; Mikli, V.; Kübarsepp, J.; Hussainova, I. *Key Eng. Mater.* **2016**, *674*, 77–80.

(23) Ferrari, A. C.; Basko, D. M. *Nat Nano* **2013**, *8*, 235-246.

(24) Peng, Z.; Wu, J.; Yang, H. *Chem. Mater.* **2010**, *22*, 1098-1106.

(25) Wu, G.; More, K. L.; Johnston, C. M.; Zelenay, P. *Science* **2011**, *332*, 443-447.

(26) Biddinger, E. J.; Ozkan, U. S. *J. Phys. Chem. C* **2010**, *114*, 15306-15314.

(27) Wildgoose, G. G.; Wilkins, S. J.; Williams, G. R.; France, R. R.; Carnahan, D. L.; Jiang, L.; Jones, T. G. J.; Compton, R. G. *ChemPhysChem* **2005**, *6*, 352-362.

(28) Cullen, R. J.; Jayasundara, D. R.; Soldi, L.; Cheng, J. J.; Dufaure, G.; Colavita, P. E. *Chem. Mater.* **2012**, *24*, 1031-1040.

(29) Hussainova, I.; Ivanov, R.; Stamatin, S. N.; Anoshkin, I. V.; Skou, E. M.; Nasibulin, A. G. *Carbon* **2015**, *88*, 157-164.

(30) Ferrari, A. C. *Solid State Commun.* **2007**, *143*, 47-57.

(31) Jorio, A. *ISRN Nanotechnology* **2012**, *2012*, 234216.

(32) Banks, C. E.; Davies, T. J.; Wildgoose, G. G.; Compton, R. G. *Chem. Commun.* **2005**, 829-841.

(33) Kim, H.; Lee, K.; Woo, S. I.; Jung, Y. *Phys. Chem. Chem. Phys.* **2011**, *13*, 17505-17510.

(34) Yuan, W.; Zhou, Y.; Li, Y.; Li, C.; Peng, H.; Zhang, J.; Liu, Z.; Dai, L.; Shi, G. *Sci. Rep.* **2013**, *3*, 2248.

(35) Nikolic, J.; Expósito, E.; Iniesta, J.; González-Garcia, J.; Montiel, V. *J. Chem. Educ.* **2000**, *77*, 1191-1194.

(36) Schmidt, T. J.; Gasteiger, H. A.; Stäb, G. D.; Urban, P. M.; Kolb, D. M.; Behm, R. J. *J. Electrochem. Soc.* **1998**, *145*, 2354-2358.

(37) Mayrhofer, K. J. J.; Strmcnik, D.; Blizanac, B. B.; Stamenkovic, V.; Arenz, M.; Markovic, N. M. *Electrochim. Acta* **2008**, *53*, 3181-3188.

(38) Stamatin, S. N.; Borghei, M.; Andersen, S. M.; Veltze, S.; Ruiz, V.; Kauppinen, E.; Skou, E. M. *Int. J. Hydrogen Energy* **2014**, *39*, 8215-8224.

(39) Wain, A. J.; Lawrence, N. S.; Greene, P. R.; Wadhawan, J. D.; Compton, R. G. *Phys. Chem. Chem. Phys.* **2003**, *5*, 1867-1875.

(40) Higgins, D. C.; Hoque, M. A.; Hassan, F.; Choi, J.-Y.; Kim, B.; Chen, Z. *ACS Catal.* **2014**, *4*, 2734-2740.

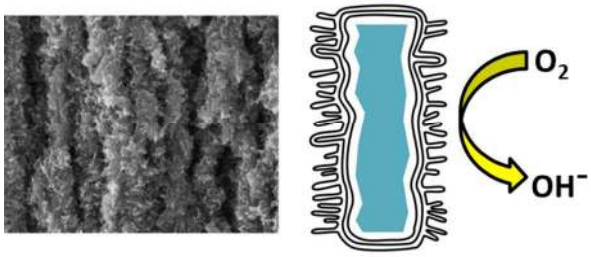
O_2
OH^-

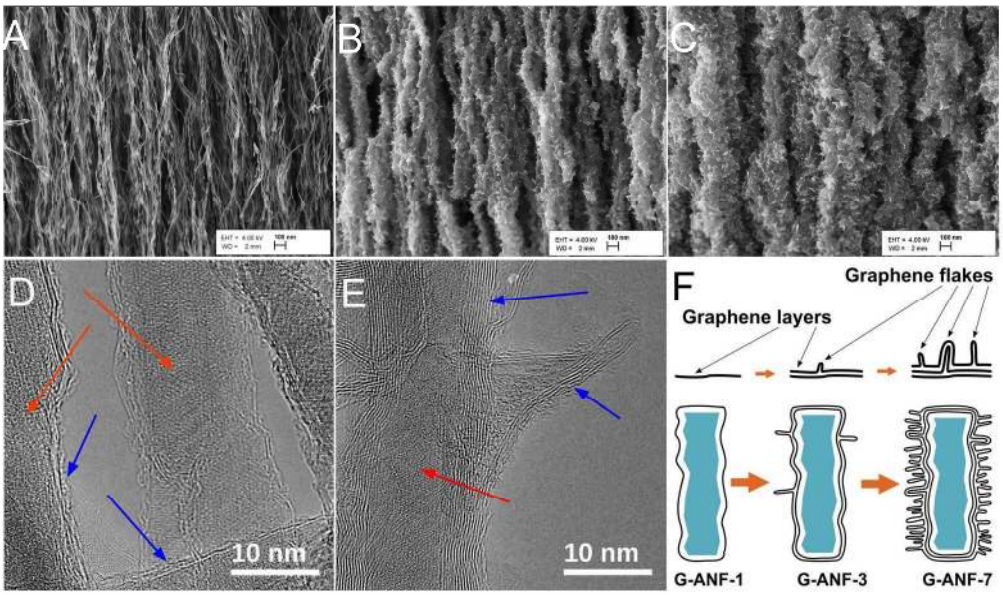

Figure 1. SEM images of G-ANF-1 (A), G-ANF-3 (B), G-ANF-7 (C) (scale bar = 100 nm); TEM images of G-ANF-1 (D) and G-ANF-3 (E) and schematic illustration of the material synthesis (F).

94x56mm (600 x 600 DPI)

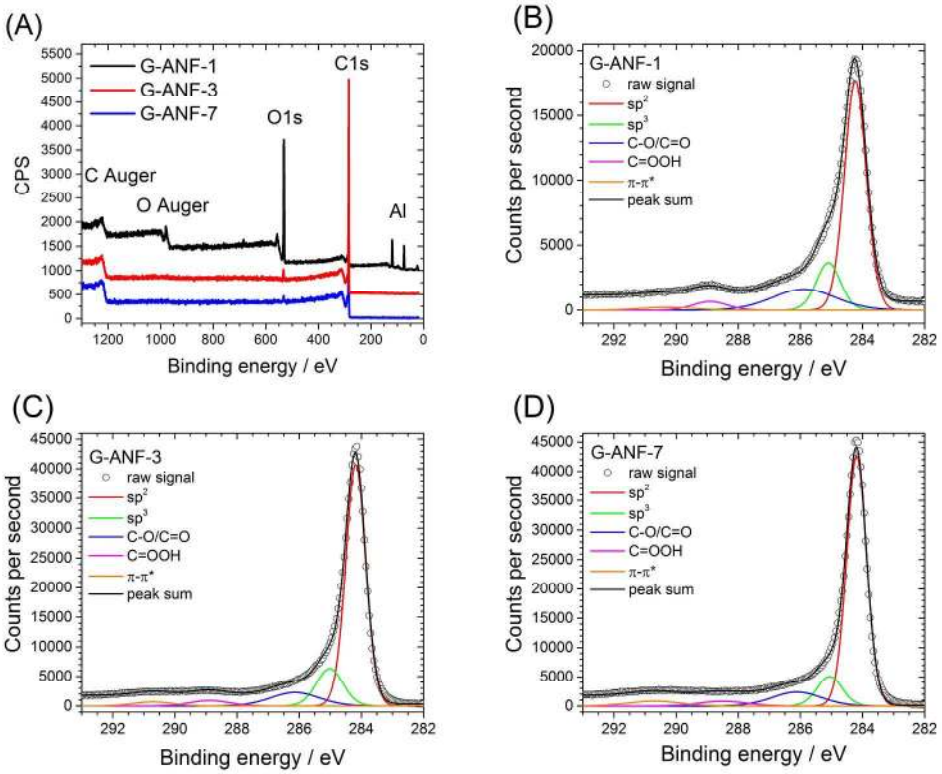

Figure 2. X-ray photoelectron spectra survey (A), high resolution of G-ANF-1 (B), G-ANF-3 (C) and G-ANF-7 (D).

124x96mm (600 x 600 DPI)

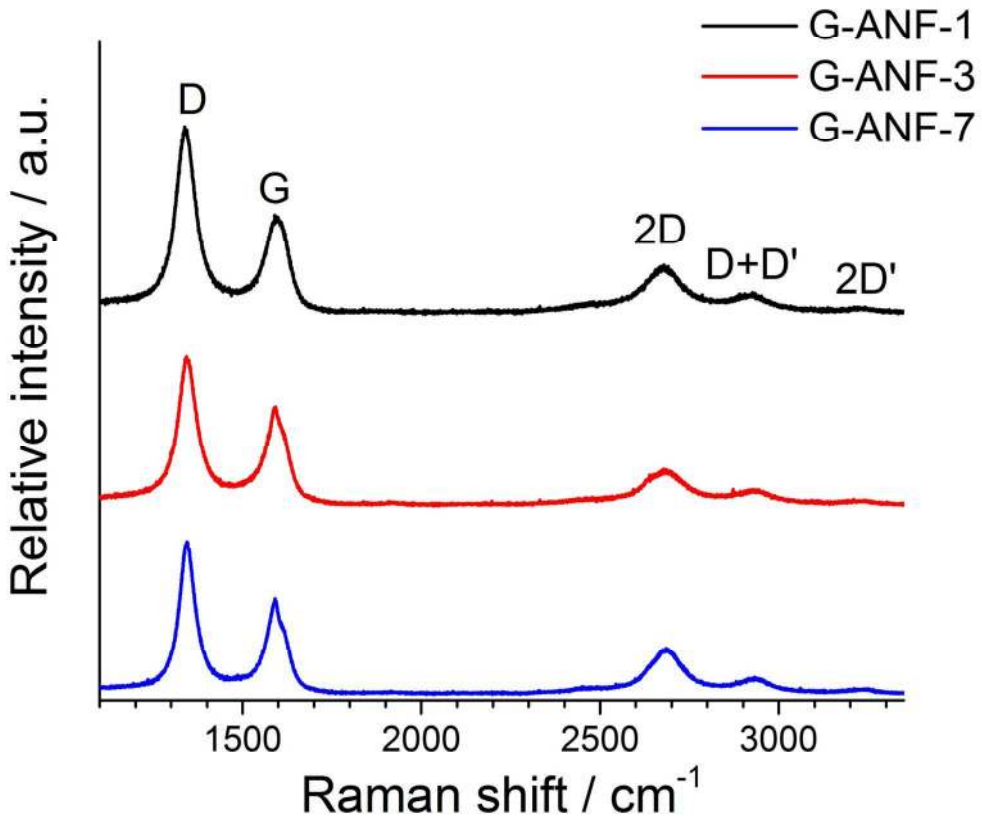

Figure 3. Raman spectra (exc. 532 nm) of G-ANF-1 (black), G-ANF-3 (red) and G-ANF-7 (blue). All spectra are normalized by the height of the G peak to facilitate comparison.

77x71mm (600 x 600 DPI)

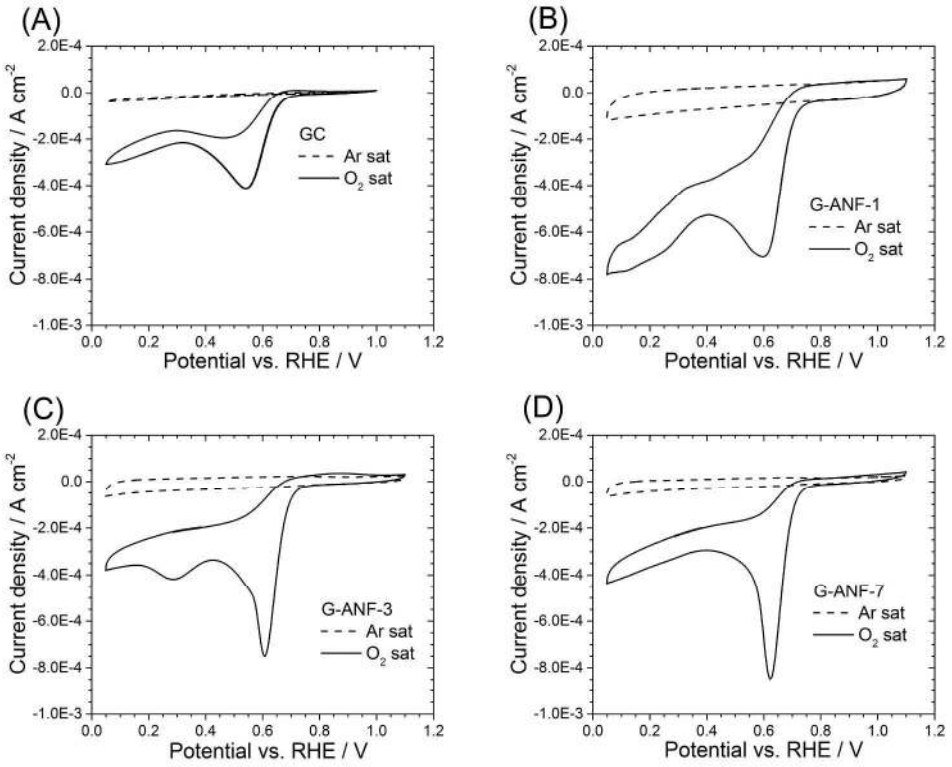

Figure 4. Cyclovoltametric scans of GC (A), G-ANF-1 (B), G-ANF-3 (C) and G-ANF-7 (D) in Ar (dashed line) and O_2 (solid line) saturated 0.1 M KOH; recorded between 0.05 and 1.1 V_{RHE} at 0.05 V s^{-1} and 25 °C.

128x99mm (600 x 600 DPI)

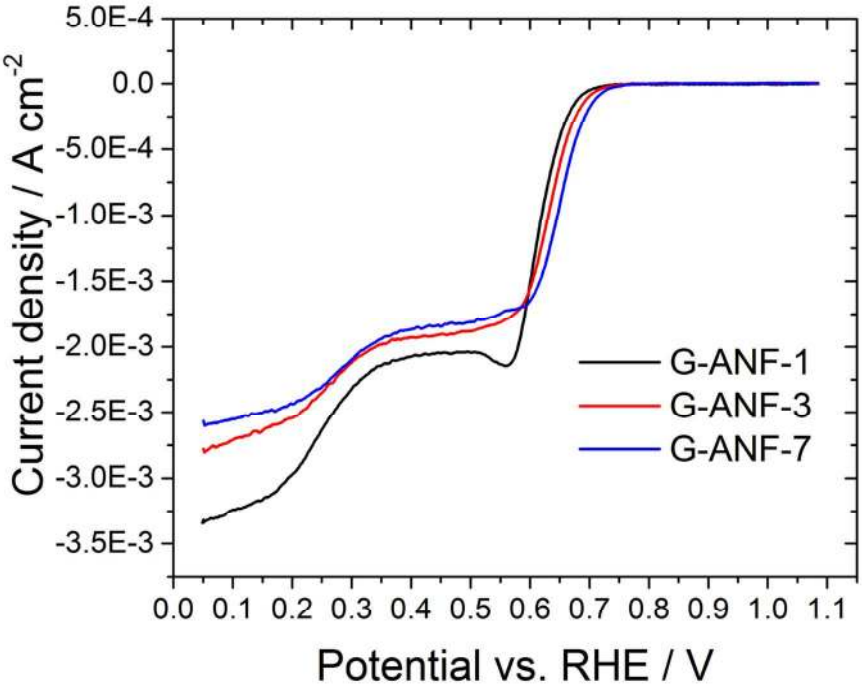

Figure 5. Cathodic voltammetric waves of G-ANF-1 (black line), G-ANF-3 (red line) and G-ANF-7 (blue line) recorded in O_2 saturated 0.1 M KOH between 0.05 and 1.1 V_{RHE} at 0.05 V s^{-1}, 900 rpm and 25 °C. All waves are shown after subtraction of capacitive contributions.

66x51mm (600 x 600 DPI)

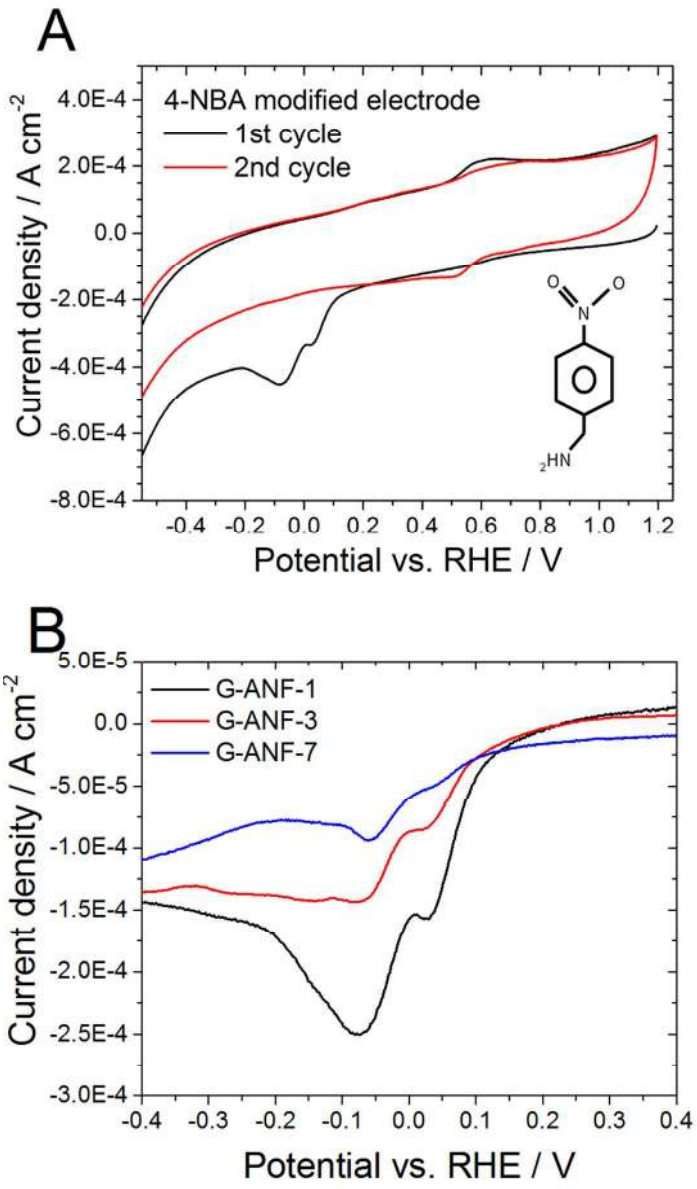

Figure 6. Cyclovoltammetric scans of a 4-NBA (inset) modified electrode (A) and 4-NBA modified G-ANF-1 (black line), G-ANF-3 (red line) and G-ANF-7 (blue line) (B) recorded in Ar saturated 0.1 M H_2SO_4 between 1.2 and -0.8 V_{RHE} at 0.2 V s^{-1}. Curves in (B) are shown after correction by background current to facilitate comparison.

83x130mm (300 x 300 DPI)

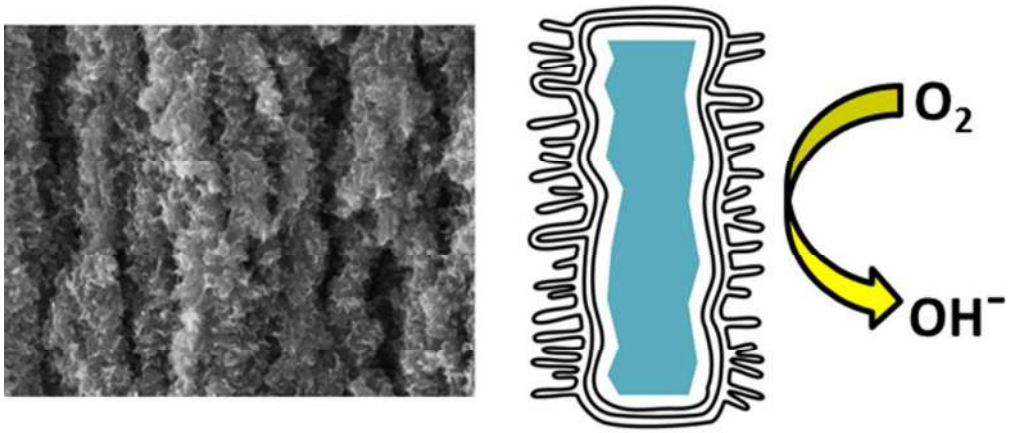

Table of Contents Graphic

77x36mm (300 x 300 DPI)